Computer Science and Information Systems 21(4):1221–1241 https://doi.org/10.2298/CSIS231230023Y

Threshold Segmentation Based on Information Fusion for Object Shadow Detection in Remote Sensing Images

Shoulin Yin[1], Liguo Wang[2,⋆], and Lin Teng[1]

[1] School of Information and Communication Engineering, Harbin Engineering University
Harbin 150001 China
yslin@hit.edu.cn
[2] College of Information and Communications Engineering, Dalian Minzu University
Dalian, 116600, China
wangliguo@hrbeu.edu.cn

Abstract. In the shadow detection task, the shadow model is usually consistent with the approximate contour of ontology semantics, it is difficult to extract the features of land covered objects or ground pixels, and easy to be confused into foreground objects in gray scale. Therefore, we present to formulate and apply one new threshold segmentation method based on information fusion for object shadow detection in remote sensing images. Firstly, object shadow pixels are screened using intensity and chromaticity information in HSI color space. Secondly, the remote sensing image is carried out by principal component analysis (PCA) to obtain the first principal component. A new shadow index is constructed using the results obtained from HSI and the first principal component. Thirdly, based on the results of the above two information fusion, a threshold segmentation model is established using the improved threshold segmentation algorithm between the maximum and the minimum threshold segmentation algorithm, so as to obtain the final object shadow detection results. Finally, affluent experiments are conducted on the datasets collected from Google Earth. The results show that the proposed object shadow detection algorithm in remote sensing images can achieve better segmentation and detection (more than 95%) effect compared with state-of-the-art methods.

Keywords: object shadow detection, threshold segmentation, information fusion, remote sensing images, HSI color space, PCA.

1. Introduction

With the rapid development of space remote sensing technology, remote sensing image is more and more widely used in urban planning, digital agriculture and resource exploration. Shadow, which reflects the spatial structure characteristics of ground objects, has always been a hot spot in the research of ground objects recognition. According to the length and irradiation Angle of the profile, the height and shape of the ground objects can be calculated, which is conducive to urban construction, remote sensing mapping and other applications [1,2]. However, shadow will also cover the ground objects, resulting in attenuation or loss of the effective information of the ground objects, which brings difficulties to the interpretation of remote sensing image target recognition, feature extraction and image matching. With the continuous development of sensor technology,

⋆ Corresponding author

sub-meter high resolution image has been more widely used in urban planning, road mapping and other fields [3-5]. In high-resolution images, the categories of objects are more precise, and the objects are easily affected by shaded areas, which makes the extraction and recognition of objects difficult. Therefore, further improving the precision and accuracy of shadow detection of high-resolution images has important application value and significance for urban planning and natural disaster assessment.

In the early days, people mainly used color transformation to detect shadow in color remote sensing images. Kumar et al. [6] used color and geometric position of image to extract shadow region. Srikantha et al. [7] carried out shadow extraction through image color region segmentation and image reproduction, combining with dynamic range compression. Zhang et al. [8] designed a shadow detection algorithm by analyzing the difference in pixel brightness values of RGB channels in shaded areas and non-shaded areas and combining the idea of seed filling with difference operators and covariance operators. Using color feature to extract shadow had certain application value, but it was not good for high-resolution image with higher complexity of features.

Because of the different characteristics of the shadow in different bands, the algebraic operation of the band can extract the shadow. Abd-El et al. [9] constructed a normalized blue-red band index to distinguish vegetation and shadow according to the difference in the decline amplitude of radiation brightness of blue and red bands in the shadow area, but this method was difficult to distinguish shadow from red and blue ground objects. Shi et al. [10] calculated the difference ratio of green and blue wave segments and extracted shadows by combining with histogram threshold segmentation of near infrared band. This method could not extract shadows effectively in complex atmospheric and ground conditions. Wang et al. [11] carried out shadow extraction through linear calculation and nonlinear calculation between bands and combined with digital elevation model. This method would cause loss of data accuracy, and the accuracy of shadow extraction was easily affected by image quality.

Ward et al. [12] proposed a radiation model based on direct light and reflected light, and used the difference of direct light and reflected light to extract shadow regions. However, this method required the height and Angle attributes of the sun, which had obvious limitations and high cost, it was not conducive to its implementation. Du et al. [13] proposed a shadow segmentation algorithm that could make use of histogram threshold, but this method had the problem of poor threshold segmentation effect. Fu et al. [14] proposed a shadow detection model using HIS changes, which used shadow index to distinguish shaded areas from non-shaded areas, but this method had a high misjudgment rate.

Therefore, we propose a novel object shadow detection threshold segmentation method based on information fusion in remote sensing images. Our main contributions are as follows.

1. Object shadow pixels are firstly screened using intensity and chromaticity information in HSI color space.
2. The remote sensing image is carried out by principal component analysis (PCA) to obtain the first principal component. A new shadow index is constructed using the results obtained from HSI and the first principal component.
3. Based on the results of the above two information fusion, a threshold segmentation model is established using the improved threshold segmentation algorithm between

the maximum and the minimum threshold segmentation algorithm, so as to obtain the final object shadow detection results.

2. Related Works

At present, some scholars have summarized some shadow detection methods. For example, Hou et al. [15] summarized and classified the existing shadow detection methods of remote sensing images, and put forward the problems of generalization and robustness that needed to be solved in the current shadow detection research. Liu et al. [16] mainly introduced several cloud detection methods for common satellite data. By comparing different shadow detection methods, they pointed out that existing methods had problems such as weak universality and missing judgment and misjudgment for thin and transparent clouds. Mahajan et al. [17] reviewed shadow detection methods from the aspects of classical algorithms and machine learning methods, compared and analyzed the detection accuracy of the two types of methods in different scenarios. Based on a large number of domestic and foreign references, this paper summarized the existing shadow detection methods into three categories: Threshold method, spatial change detection method and machine learning method. Threshold method is a widely used shadow detection method, such as the early shadow coverage extraction of single image [18], pixel level shadow detection for a series of Landsat satellites [19], and the new Sentinel-2 satellite shadow detection. The Fmask (Function of mask) algorithm proposed by Zhu et al. [20] had been integrated into the basic remote sensing camera processing flow of U.S. Geological Survey (USGS). The spatial change detection method used the spatial change information of multi-period images to achieve higher cloud detection accuracy than that of a single image [21]. Machine learning methods include traditional machine learning methods, such as Support Vector Machine (SVM), Artificial Neural Network (ANN), Random Forest (RF), etc. It also includes the most popular methods of deep learning. Among them, traditional machine learning methods are trained through a large number of training sets, and the trained classifier is used to separate shadow pixels and clear sky pixels [22,23]. However, the deep learning method is driven by a large number of marked samples of shadows and adopts an algorithm framework with semantic information extraction and learning such as convolutional neural network to achieve the purpose of shadow detection [24].

2.1. Thresholding Method

The threshold method is to separate the cloud and the ground object by using the different spectral characteristics of the cloud and the underlying surface, and compare the detected value of the pixel with the threshold value to determine whether it is the ground object or the cloud. The key of this method lies in the determination of threshold. In the early stage, most of them are fixed threshold method. Later, dynamic threshold, adaptive threshold and multi-band combination threshold are developed, and different thresholds can be selected according to different conditions. In recent years, the threshold method has been further developed on the basis of the existing development. For example, based on the Fmask (Function of Mask) algorithm, the Fmask 4.0 algorithm [25] is further developed to improve the cloud detection method. The improvement mainly includes three

aspects: First, the integration of auxiliary data, in which the Global Surface Water Occurrence (GSWO) data is used to improve the separation of land and water, and the global digital elevation model is used to standardize the tropical and cirrus zones. Second, a new cloud probability is developed, which uses the cloud probability based on Haze Optimized Transformation (HOT) to replace the temperature probability of Sentinel-2 image, and then corrects the global optimal threshold of cloud probability for different sensors. The Spectral Context-Contextual Snow Index (SCSI) is created to better differentiate snow/ice and clouds in polar regions. Landsat 4-8 and Sentinel-2 data are used for training and verification, and the results show that the overall accuracy of Fmask 4.0 algorithm is higher than that of Fmask algorithm. Different from Fmask 4.0 Algorithm, which used fixed threshold to perform cloud detection, Chang et al. [27] proposed an improved cloud detection algorithm-generating (CDAG) method based on automatic threshold. According to the characteristics of GF-6 WFV data, the CDAG method is improved from the two aspects of adding bright surface pixel database and band combination. The results show that the improved CDAG cloud detection algorithm can achieve better recognition effect in the cloud recognition of GF-6 WFV data. However, due to the lack of short-wave infrared band of GF-6 WFV sensor, the improved CDAG method cannot identify cloud pixels in ice and snow regions. In summary, the threshold method is simple, high computation speed and easy to implement. However, its disadvantage is that the setting of threshold requires more prior knowledge and human participation, and the subjectivity is strong. Moreover, different strategies and thresholds are required for images taken by different sensors, different periods or places, which limits the universality of the method.

In addition to the spectral information, the spatial information of the image can also be used as the feature to set the threshold method for cloud detection. With the continuous improvement of spatial resolution of remote sensing images, cloud texture presents unique characteristics. Fractal dimension and gray co-occurrence matrix can be used to quantitatively express texture features. Fractal dimension is used to describe the complexity of fractals. In remote sensing images, the complexity of ground objects is higher than that of clouds, so the fractal number of ground objects is greater than that of clouds, so as to distinguish the two. The angular second order moments in the gray co-occurrence matrix reflect the texture law. Clouds in the image have larger angular second order moments than ground objects, which can distinguish them. Xu et al. [27] proposed a cloud detection algorithm combining spectral threshold and texture features, and used this algorithm to detect the cloud of hyperspectral remote sensing images captured by the Hyperion sensor of EO-1 satellite, which not only greatly improved the cloud detection accuracy of remote sensing images, but also met the requirements of fast cloud detection of space-borne hyperspectral images. In addition, Calin et al. [28], aiming at cloud detection in infrared images, adopted a method combining fractal dimension and gray co-occurrence matrix to effectively realize cloud detection in infrared images. Due to the complexity of cloud spatial information, cloud detection methods based on cloud texture characteristics were easy to cause a small number of clouds in the image to be missed, resulting in certain errors.

2.2. Spatial Change Detection Method

The presence of cloud on remote sensing image will significantly affect the radiation change of image, which is the basis of cloud detection based on spatial change. The prin-

ciple of spatial change detection method is to detect clouds and shadows by using the temporal characteristic changes of multi-temporal remote sensing images. For example, Zhang et al. [29] proposed the Multi-Temporal Cloud Detection (MTCD) method. The cloud detection results of FORMOSAT-2 and Landsat 5, 7 remote sensing images were better than those of artificial labels. However, MTCD required time series images and had high requirements on images, so its application in some sensors was limited. Zhang et al. [30] proposed the Multi-Temporal mask method, an automatic detection algorithm for cloud/cloud shadow and snow in multi-temporal landsat images. Based on the Fmask method, the time information of cloud-free pixels in multi-temporal remote sensing images was added to improve the cloud detection accuracy. Automatic time-series Analysis (ATSA) used the unsupervised classification method to detect clouds in time series images, and analyzed the geometric relationship between the sun's azimuth Angle, altitude Angle and clouds to detect cloud shadows. In the cloud detection experiment of multi-sensor remote sensing images, the detection effect of ATSA method was superior to that of Fmask. Sorasak etc. [31] presented Multi-temporal Cloud Masking (MCM) method, the method was used in tropical and subtropical environment Landsat 8 cloud/cloud shadow detection. Compared with Landsat 8 Cloud Cover Assessment (L8CCA) proposed by Candra et al. [32], MCM method could achieve higher accuracy. In addition, Qiu et al. [33] developed a cloud detection method with Cirrus cloud mask (Cmask), which used cirrus band (spectrum range 1.36-1.39) to detect cirrus cloud in Landsat 8 time series images [34].

Compared with the threshold method, on the one hand, the spatial change detection method adds time information into the cloud detection process, which makes the method more suitable for cloud detection of time series remote sensing images. On the other hand, because the method relies on time information for detection, the application scenario of this method is limited.

2.3. Temporal Substitution Method

With the rapid development of data fusion technology, cloud removal methods based on multi-phase image replacement also have a certain development. The cloud removal method based on multi-phase image replacement uses cloudless pixels to replace cloudless pixels according to certain principles to achieve the purpose of generating clear sky images. For example, the Closest Spectral Fit (CSF) [35] cloud removal method, which used cloud images and cloud-free images taken at different times in the same region to replace pixels to achieve cloud removal. CSF achieved high accuracy in cloud removal for Landsat and Quick Bird images. Moreover, the accuracy of the method was not affected by the size, thickness and density of the cloud. Similar to the principle of CSF, Liu [36] replaced the cloudless pixel in Radarsat-2 fully polarized SAR image with the least spectral difference from the pixel with cloud region in Landsat 8 OLI false color image by weighted Euclidean distance, and realized cloud noise removal and repair in Landsat 8 remote sensing image. This method could integrate the advantages of microwave and optical images to achieve cloud region restoration of multi-spectral images and achieve a better cloud removal effect. In addition, Huang et al. [37] proposed a method to reconstruct cloud region information by using the correlation of multi-temporal images. First, images at different times were obtained with similar cloud-free patches to reconstruct cloud pollution regions, and then Poisson equation was used to globally optimize the filled cloud

images to improve the radiation inconsistency problem. Li et al. [38] further proposed a joint determination method to replace Poisson equation to reconstruct and optimize cloud pollution images. Compared with the original method, the optimized method performed better in terms of radiation accuracy and consistency. Ji et al. [39] proposed an automatic cloud removal algorithm, which firstly used temporal similarities of multi-temporal Landsat images to reconstruct the cloud polluted part, and then adopted Poisson hybrid algorithm to further eliminate the radiation difference between the cloud-free region and the reconstructed region. The algorithm automatically generated a cloud-free dataset for Landsat 8 from 2013 to 2017, covering the whole of China, and the method could also generate cloud-free time series images for other satellites.

The cloud removal method based on multi-phase image replacement can make full use of existing images to achieve the purpose of cloud removal, but the prerequisite for the application of this method is not only to solve the registration and correction problems between different images, but also to solve the radiation difference between the original image and the corrected image, and to ensure that multiple sensors obtain remote sensing data in the same area, which is very demanding.

3. Proposed Object Shadow Detection Model

Considering the accuracy and real-time detection requirements, this paper presents an object shadow detection threshold segmentation method based on information fusion. The detailed detection structure is shown in Figure 1.

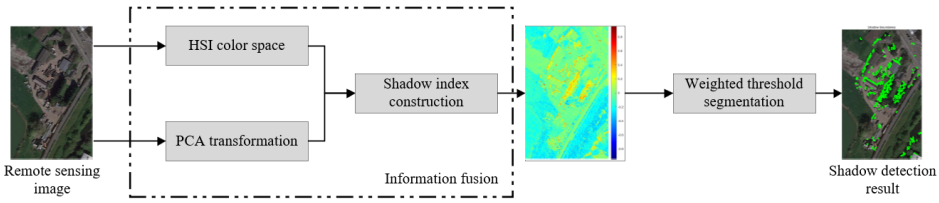

Fig. 1. Proposed detection flowchart

3.1. HSI Color Space Transformation

According to lighting model in reference [40], the brightness of an object mainly comes from ambient reflected light, diffuse reflected light and specular reflected light, which can be expressed as:

$$I = I_a k_a + I_p k_d \cos\theta + I_p k_s \cos^n \varphi. \tag{1}$$

Where I_a is the ambient brightness. k_a is the ambient reflection coefficient of the object surface. I_p is the intensity of direct light source. k_d and k_s are the diffuse and specular reflection coefficients of the object surface to the light source, respectively. θ is

the incidence Angle of the direct light source. φ is the Angle between the mirror reflection direction and the camera observation direction. n is the convergence index of specular reflected light. When the direct light in the scene is partially or completely blocked by the object and the shadow appears, the diffuse reflection and specular reflection of the direct light source in the area will be significantly reduced, so the brightness of the shadow area can be expressed as:

$$I' = I_a k_a + \lambda I_p (k_d \cos\theta + k_s \cos^n \varphi) < I. \tag{2}$$

Where, $0 < \lambda < 1$, whose size is determined by the spatial position of the pixel or area in the scene. Through the above analysis, it can be found that a prominent feature before and after the shadow appears in the background area is that the brightness of pixels in the current frame is lower than that of corresponding pixels in the background, so the shadow can be screened by brightness changes.

The perceived color characteristics of an object depend on the spectral reflection characteristics of the object surface, independent of changes in the scene and light. When the brightness of an object changes, the color information perceived by human eyes is basically unchanged, that is, chroma is independent of brightness. For example, the normalized color feature RGB in rgb space, UV component in YUV space, hue H and saturation S in HSI space, etc. Therefore, it is possible to distinguish the target from the shadow by using the approximately identical chromaticity of the pixel in the shadow area and the corresponding background area.

HSI color space clearly expresses Hue, Saturation and Intensity changes and greatly simplifies the workload of image analysis and processing. Therefore, this paper selects HSI color space for preliminary screening of shadows. According to the above analysis of color characteristics, compared with the corresponding background region, the brightness information of the shadow will change greatly, while the hue H and saturation S remain basically unchanged. According to the above characteristics, shadow pixels can be detected by satisfying equation (3), i.e.,

$$S_1 = \begin{cases} 127 & \alpha_1 \le P_F^i / P_B^i \le \alpha_2 \\ 255 & others \end{cases} \tag{3}$$

Here, $|P_F^h - P_B^h| \le \beta$, $|P_F^s - P_B^s| \le \gamma$. S_1 is the screened shadow region. h, s and i respectively represent hue, saturation and brightness after the normalization of HSI color space. P_F^h, P_F^s, P_F^i and P_B^h, P_B^s, P_B^i represent h, s and i values corresponding to pixel point P in the current detection image F and background image B respectively. α_1, α_2, β and γ are the shadow discrimination thresholds of each color component. Threshold setting is to select the weak threshold from the optimal threshold range obtained by manual experiment, so as to screen out the shadow area more adequately.

3.2. Principal Component Normalization Method

Principal component analysis method can reduce the dimension of data and reduce the redundancy of data [41,42]. For different remote sensing images, different bands can be selected for principal component analysis. Different eigenvalues can be obtained by principal component analysis of different wavebands. The larger eigenvalue denotes the better corresponding eigenvector. For remote sensing images, since the variance contribution

rate of the first principal component is usually above 90%, the first principal component image can represent most of the information of the original image. The original image and the first principal component image are shown in Figure 2.

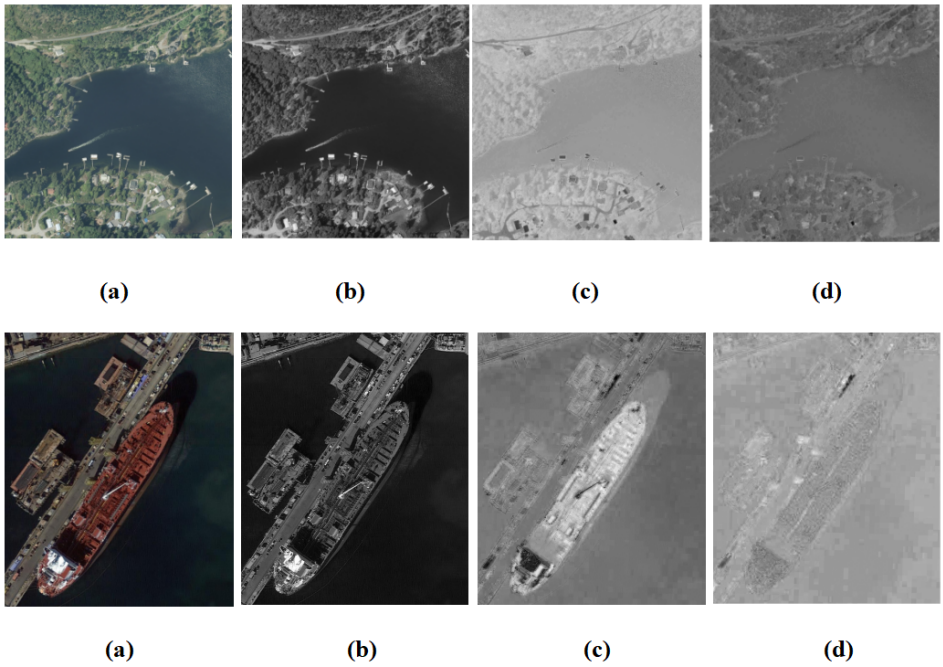

Fig. 2. Diagram of principal component analysis results. (a) original image; (b) First principal component image; (c) Second principal component image; (d) Third principal component image

As can be seen from Figure 2(b), after principal component transformation, the brightness of the shadow region is greater than that of other ground objects, which is conducive to further shadow extraction. According to ENVI analysis, the shadow region is always at both ends of the first principal component, that is, at the maximum value of positive value and the minimum value of negative value. Therefore, normalization of the first principal component within [0,1] can better highlight the difference between shadows and other features.

3.3. Shadow Index Construction

After the color component C is extracted from the remote sensing image through HSI conversion of color space, the blue light value of the shadow area is larger than that of the red and green light value, which enhances the contrast with other ground objects. After principal component transformation of remote sensing image, the shadow region is located

at two endpoints of the first principal component. Through normalization, the shadow region occupies a larger value in the first principal component than other features, which is similar to the C component. Inspired by the similarity, this paper proposes a shadow index construction method combining C component and first principal component. The shadow index is expressed as follows:

$$shadow - index = \frac{C - PC1}{C + PC1}. \tag{4}$$

3.4. Weighted Threshold Segmentation

In the task of shadow detection, in order to detect the shadow region more conveniently, the three channels of RGB image are first separated to obtain the single channel information of R, G and B, and then the linear weighting algorithm of Equation (5) is used for information fusion processing between channels. Set the three channels of remote sensing image as R, G and B respectively, then the weighted gray value I_{gray} is:

$$I_{gray} = 0.2R(x, y) + 0.6G(x, y) + 0.2B(x, y). \tag{5}$$

After gray linear processing, the pixel intensity of the shadow part is lower than that of the non-shadow area. With the gray level intensity of 0-255 pixels as the horizontal coordinate and the frequency of each gray level pixel intensity as the vertical coordinate, the functional statistical mapping relationship between gray level intensity frequency and gray level intensity in remote sensing images is established.

In the gray distribution diagram (Fig.3 (d)), the area with low gray level is the shadow area, while the area with high gray level is the non-shadow area. The gray value changes of the shaded area are more concentrated, and the distribution range of the non-shaded area is more extensive than that of the shaded area. The trough between two crests is used as the threshold to segment the shadow region, although it can be recognized, but the segmentation and recognition effect is poor. At present, the most common method is to establish the threshold segmentation model based on pixel intensity by using the maximum inter-class variance method, and determine a threshold by using the threshold segmentation model adaptively. However, the method of determining the boundary threshold between shadow and non-shadow regions based on the maximum inter-class variance only describes the variance distance between shadow and non-shadow categories, and does not take into account the differences within each category. In this paper, a constraint term of minimum in-class variance is added to the maximum category variance. First, it calculates the maximum variance distance needed to distinguish between the two categories. The larger distance denotes the better the classification effect of shadow and non-shadow. Then it calculates the minimum variance distance between the elements in each class. The smaller minimum variance distance denotes the more dense the elements in the class, indicating that the probability of each gray pixel belonging to the same category is greater. The detailed steps are as follows.

1. Set the gray value interval of the shadow region and the non-shadow region in the remote sensing image as $[0, m]$, then the number of gray values of all pixels is shown

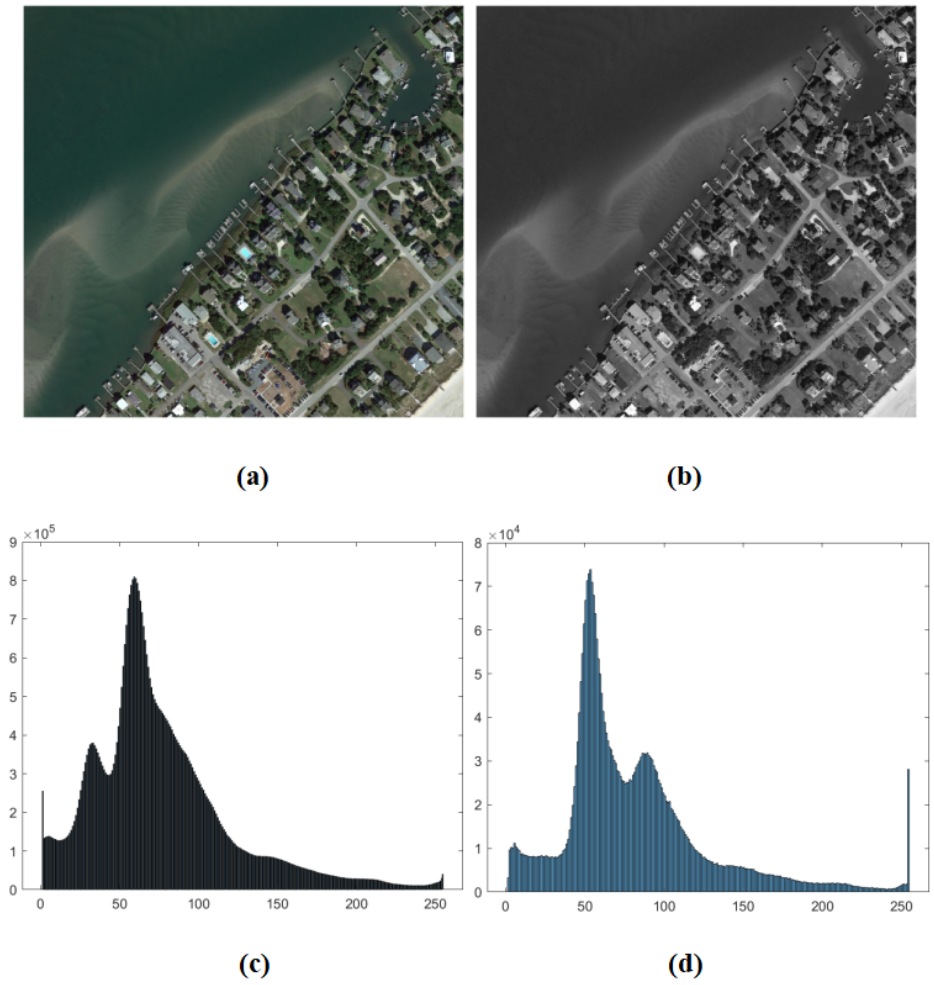

Fig. 3. Gray value distribution map. (a) original image; (b) Grayscale linear processing graph; (c) One-dimensional histogram of (a); (d) One-dimensional histogram of (b)

in Equation (6), the probability of each gray level is shown in Equation (7), and the overall gray mean μ_{all} is shown in Equation (8):

$$N = \sum_{i=0}^{m} h(i). \tag{6}$$

$$p_i = \frac{h(i)}{N}. \tag{7}$$

$$\mu_{all} = \frac{\sum_{i=0}^{m}(h(i) \times i)}{\sum_{i=0}^{m} h(i)}. \tag{8}$$

Where i is the gray level of the gray distribution map. $h(i)$ is the frequency corresponding to the gray level i. m is the maximum gray level of the gray distribution diagram (255 in this paper). μ_{all} indicates the global average gray level.

2. Let T be any gray value of the interval $[0, m]$. T is used as the segmentation threshold, and the image of shadow area and non-shadow area is divided into gray interval $[0, T]$ and $[T+1, m]$, which are denoted as $C1$ and $C2$ respectively. Formula (9) and formula (10) are used to calculate the average gray level μ_{C1} and μ_{C2} of the two parts respectively.

$$\mu_{C1} = \frac{\sum_{i=0}^{T}(h(i) \times i)}{\sum_{i=0}^{T} h(i)}. \tag{9}$$

Where i is the gray level of the dark pixel in the shadow area in the gray distribution map. $h(i)$ is the corresponding frequency of gray level i of dark pixel in shadow region. T is the threshold of boundary between shadow area and non-shadow area. μ_{C1} is the average gray level of $C1$ region.

$$\mu_{C2} = \frac{\sum_{i=T+1}^{m}(h(i) \times i)}{\sum_{i=T+1}^{m} h(i)}. \tag{10}$$

Where i is the gray level of bright pixels in the non-shadow area of the gray distribution map. $h(i)$ is the corresponding frequency of gray level i of bright pixel in non-shadow area. T is the threshold of boundary between shadow area and non-shadow area. μ_{C2} is the average gray level of the $C2$ region.

3. Equations (11-14) are used to calculate the variances of $C1$ in the dark shadow region and $C2$ in the bright non-shadow region respectively.

$$w_{C1} = \sum_{i=0}^{T} p(i). \tag{11}$$

$$w_{C2} = \sum_{i=T+1}^{m} p(i). \tag{12}$$

$$\sigma_{C1} = \frac{\sum_{i=0}^{T}(i - \mu_{C1})^2 \times h(i)}{\sum_{i=0}^{T} h(i)}. \tag{13}$$

$$\sigma_{C2} = \frac{\sum_{i=T+1}^{m}(i - \mu_{C2})^2 \times h(i)}{\sum_{i=T+1}^{m} h(i)}. \tag{14}$$

4. Formula (15) is used to calculate the maximum intra-class variance, maximum inter-class variance and the optimization evaluation function. The maximum intra-class variance σ_w at the threshold T is:

$$\sigma_w = w_{C1}\sigma_{C1} + w_{C2}\sigma_{C2}. \tag{15}$$

The maximum inter-class variance σ_b at the threshold T is:

$$\sigma_b = w_{C1}(\mu_{C1} - \mu_{all})^2 + w_{C2}(\mu_{C2} - \mu_{all})^2. \tag{16}$$

To ensure the optimal segmentation threshold, two conditions are required: one is that the variance between the shaded part and the non-shaded part is the largest; the other is that the variance within the shaded area and the non-shaded area is the smallest. In order to describe this phenomenon, the segmentation optimization function is defined:

$$\zeta(T) = max(\sigma_b(T)/\sigma_w(T)). \tag{17}$$

Where ζ is the optimization factor, and the iterative method is used to traverse all gray levels, then the threshold T corresponding to the largest optimization factor is the optimal segmentation threshold.

5. Set the above threshold T [43], and use Equation (18) to segment the image:

$$Segmentation = \begin{cases} 255 & Optimalthreshold > T \\ 0 & otherwise \end{cases} \tag{18}$$

4. Experiments and Analysis

After analyzing the experimental process and data, the accuracy rate (ACC) and false detection rate (FDR) are selected as the evaluation indexes of remote sensing image shadow detection effect [44,45]. The data set for this article is derived from Google Earth and DOTA [46]. Due to the limited content space, we choose four sets of images as experimental results analysis. Figure 4 is the sample data set.

Firstly, we obtain the one-dimensional and two-dimensional histogram of the four samples, in order to understand the pixel distribution of the original image more clearly. The results are shown in figure 5 and figure 6. The results show that the distribution of pixels in the original image is very uneven.

Figures 7,8,9 show the color map, threshold segmentation diagram and shadow detection effect diagram with the proposed algorithm in four scenes.

This paper is compared with three advanced shadow detection methods including DUS [47], MUSA [48], MUCS [49]. Table 1 shows that the accuracy rate and false detection rate of the proposed method on the data set are superior to the other three methods. It can be seen from the data in Table 1 that the shadow detection results in this paper are better than other methods.

For image 1, the accuracy of the proposed method is 95.4%, which is 6.0%, 4.1% and 7.1% higher than that of other methods, respectively. The FDR values of DUS, MUSA and MUCS are 12.51, 9.45 and 7.28 respectively, which are 6.29, 3.33 and 1.16 higher than that of the presented method in this paper (6.12). For image 2, ACC values of DUS,

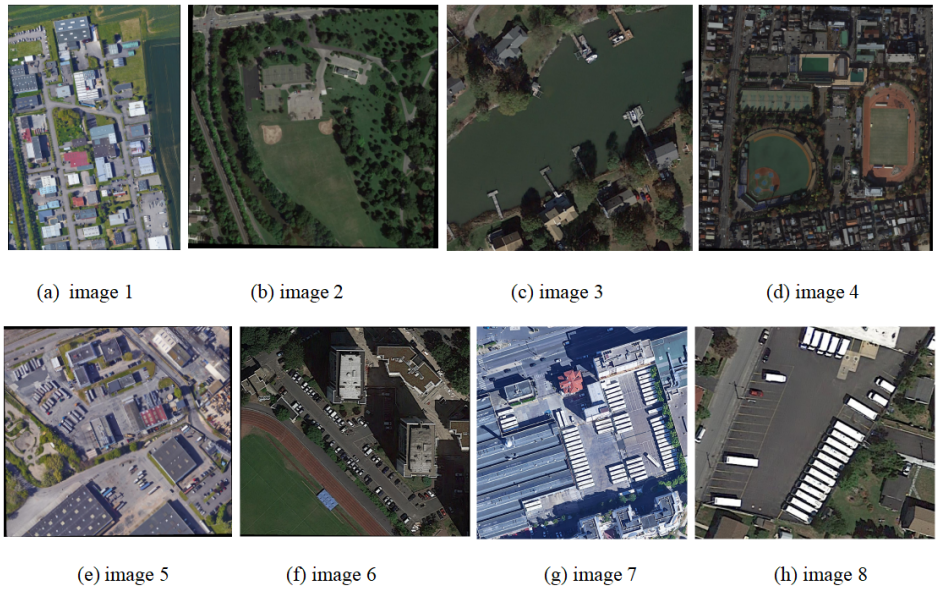

Fig. 4. Sample images

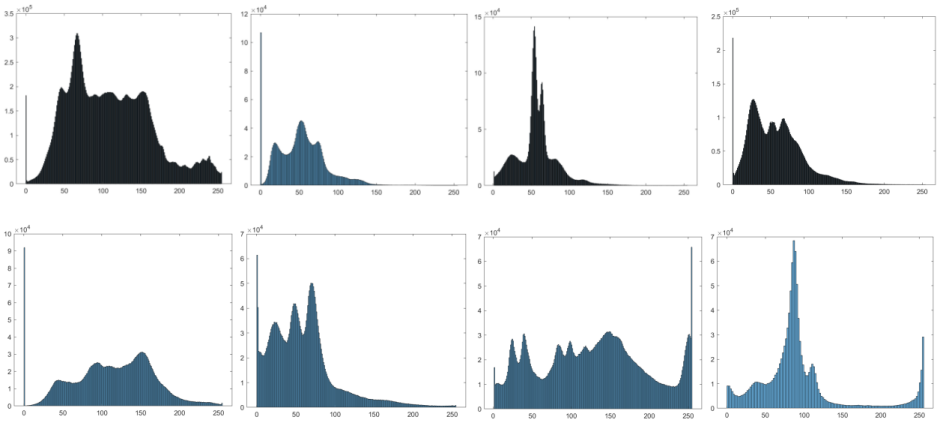

Fig. 5. One-dimensional histogram

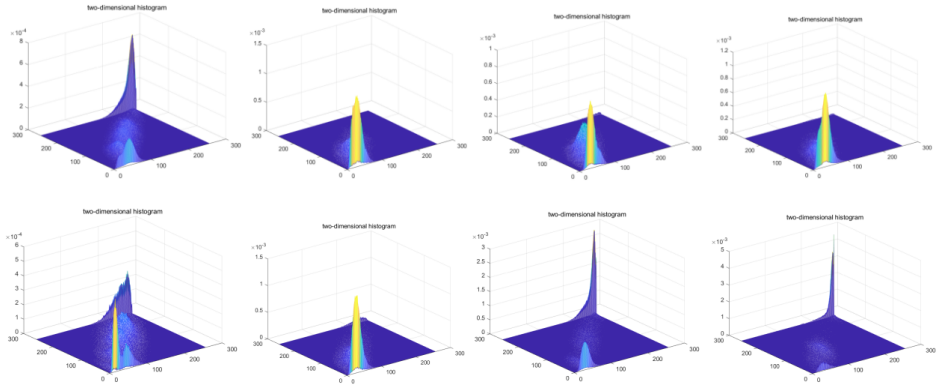

Fig. 6. Two-dimensional histogram

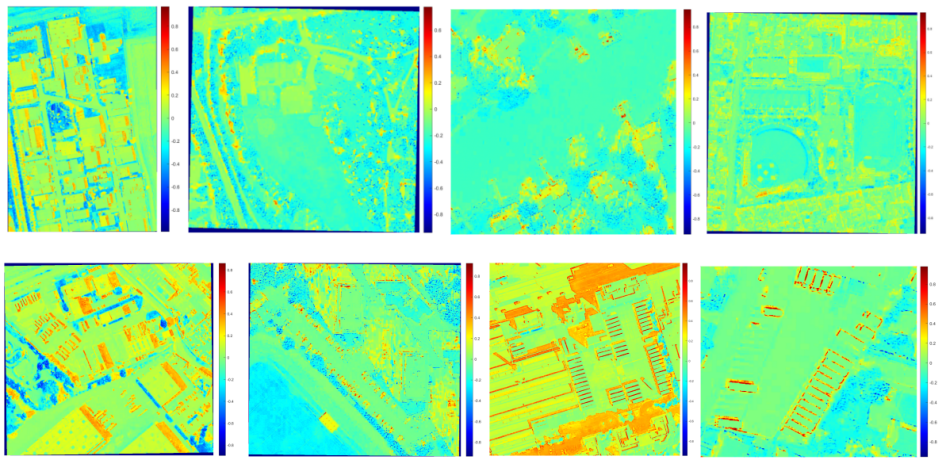

Fig. 7. Colour map

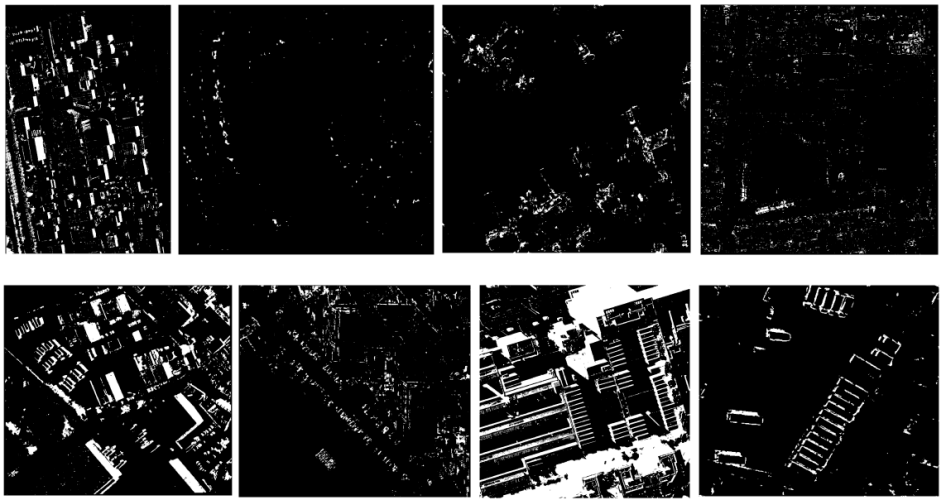

Fig. 8. Threshold segmentation

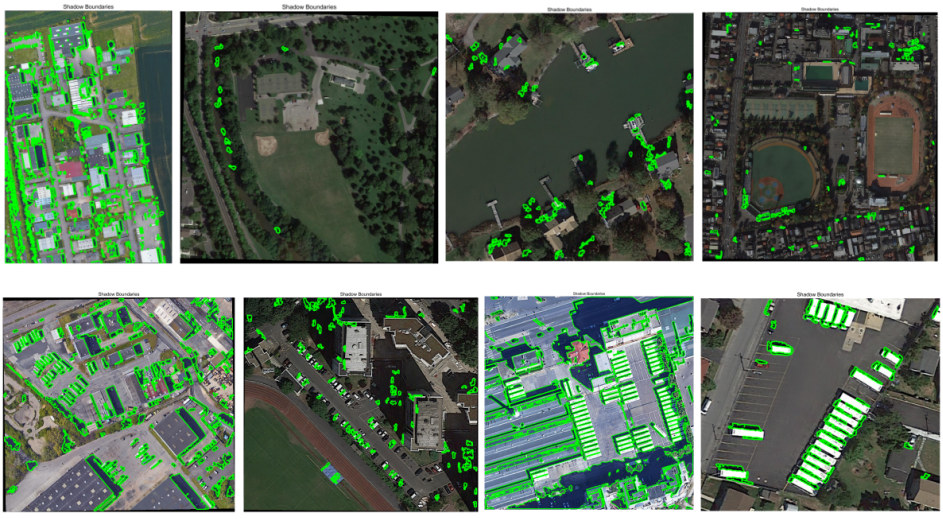

Fig. 9. Shadow detection result

Table 1. Comparison with other detection methods

Test image	Index	DUS	MUSA	MUCS	Proposed
Image1	ACC	0.894	0.913	0.937	0.954
Image1	FDR	12.51	9.45	7.28	6.12
Image2	ACC	0.875	0.886	0.907	0.935
Image2	FDR	17.32	14.81	10.64	9.78
Image3	ACC	0.907	0.928	0.935	0.961
Image3	FDR	14.69	11.58	10.44	8.94
Image4	ACC	0.863	0.892	0.917	0.934
Image4	FDR	18.52	16.74	13.55	10.95
Image5	ACC	0.906	0.915	0.921	0.946
Image5	FDR	11.85	9.93	8.31	7.25
Image6	ACC	0.885	0.891	0.907	0.922
Image6	FDR	13.25	11.74	9.33	7.21
Image7	ACC	0.927	0.939	0.951	0.960
Image7	FDR	11.24	8.11	7.58	6.93
Image8	ACC	0.902	0.927	0.933	0.958
Image8	FDR	12.35	11.26	9.75	7.07

MUSA, MUCS and proposed method are 87.5%, 88.6%, 90.7% and 93.5%, respectively. Obviously, the proposed method has some advantages over the other three methods. The FDR value of the method in this paper is 9.78, which is significantly lower than the other three methods. Similarly, in the other 7 images, the new method in this paper also has a similar trend. Also, we can see similar characteristics from Figure 10.

The running efficiency of the algorithm is also an important index to evaluate the performance of the algorithm. In order to measure the running efficiency of the algorithm proposed in this paper, the running time of different methods is given in Table 2. The visualized result is shown in Figure 11.

Table 2. Detection time with different methods/s

Test image	size	DUS	MUSA	MUCS	Proposed
Image1	2610×3931	5.71	4.66	4.25	3.36
Image2	936×913	3.04	2.89	2.37	1.24
Image3	1104×1103	4.71	3.47	2.86	2.35
Image4	1648×1732	3.97	3.65	3.17	2.83
Image5	1112×1026	4.56	3.74	3.25	2.84
Image6	1113×1015	3.75	3.23	2.77	2.51
Image7	1289×1302	3.82	3.31	2.86	2.55
Image8	673×594	3.87	3.19	2.64	2.36

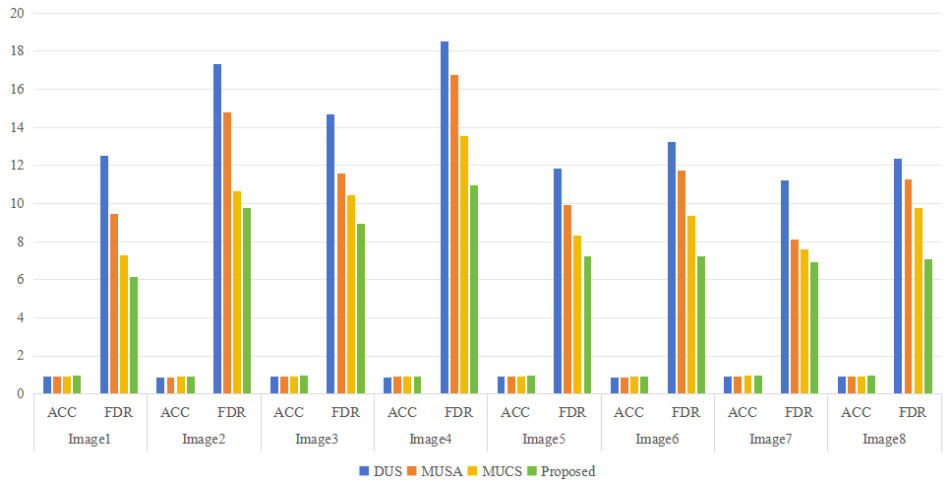

Fig. 10. Evaluation index comparison results

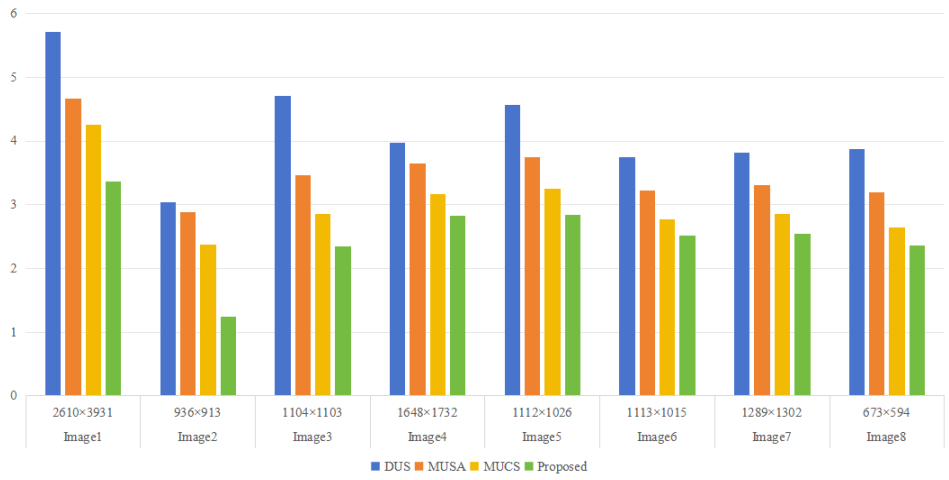

Fig. 11. Results of Table 2

5. Conclusions

Aiming at the low accuracy and robustness of shadow detection under single feature, one new threshold segmentation method based on information fusion for object shadow detection is presented in remote sensing images. Firstly, object shadow pixels are screened using intensity and chromaticity information in HSI color space. Secondly, the remote sensing image is carried out by principal component analysis (PCA) to obtain the first principal component. A new shadow index is constructed using the results obtained from HSI and the first principal component. Thirdly, based on the results of the above two information fusion, a threshold segmentation model is established using the improved threshold segmentation algorithm between the maximum and the minimum threshold segmentation algorithm, so as to obtain the final object shadow detection results. Finally, affluent experiments are conducted on the datasets collected from Google Earth. Experiments show that the proposed algorithm can accurately and quickly detect the shadow parts in the former scenic area, and has good robustness to the situation where the scene illumination changes or the local texture of the object is not obvious, which lays a good foundation for the accurate tracking and recognition of the target in the later stage.

Overall, the current cloud detection methods still have some limitations, and some areas need to continue to improve. In terms of cloud detection, there is almost no general algorithm that can detect cloud and cloud shadow on sensors, and different methods have different application conditions and scopes. Because some large-scale tasks require massive remote sensing image data, especially in some tasks that require intensive time series data and require multi-sensor data to work together, the existing cloud/shadow detection methods are limited in scope of application and poor in generalization. In addition, the accuracy of cloud detection will be affected by the background information of remote sensing images, such as ice and snow, which often cause misjudgment and missing judgment during detection, and the robustness is poor. In order to achieve a better cloud detection effect, auxiliary images with sufficient time continuity and non-overlapping cloud regions are needed, and the application prerequisite is high. At the same time, the problem of image registration and calibration across sensors and radiation difference between images should be solved.

Acknowledgments. This work was supported by the National Natural Science Foundation of China under Grants 62071084 and 62001434. The author is grateful for the anonymous review by the review experts.

References

1. Rodriguez-Moreno F, Kren J, Zemek F, et al. Advantage of multispectral imaging with sub-centimeter resolution in precision agriculture: generalization of training for supervised classification[J]. Precision Agriculture, 2017, 18: 615-634.
2. Sishodia R P, Ray R L, Singh S K. Applications of remote sensing in precision agriculture: A review[J]. Remote Sensing, 2020, 12(19): 3136.
3. Almeida L P, Almar R, Bergsma E W J, et al. Deriving high spatial-resolution coastal topography from sub-meter satellite stereo imagery[J]. Remote Sensing, 2019, 11(5): 590.
4. Moortgat J, Li Z, Durand M, et al. Deep learning models for river classification at sub-meter resolutions from multispectral and panchromatic commercial satellite imagery[J]. Remote Sensing of Environment, 2022, 282: 113279.

5. Wohlfeil J, Hirschmller H, Piltz B, et al. Fully automated generation of accurate digital surface models with sub-meter resolution from satellite imagery[J]. The International Archives of the Photogrammetry, Remote Sensing and Spatial Information Sciences, 2012, 39: 75-80.
6. Kumar S, Kaur A. Algorithm for shadow detection in real-colour images[J]. International Journal on Computer Science and Engineering, 2010, 2(07): 2444-2446.
7. Srikantha A, Sidib D. Ghost detection and removal for high dynamic range images: Recent advances[J]. Signal Processing: Image Communication, 2012, 27(6): 650-662.
8. Zhang H, Sun K, Li W. Object-oriented shadow detection and removal from urban high-resolution remote sensing images[J]. IEEE transactions on geoscience and remote sensing, 2014, 52(11): 6972-6982.
9. Abd-El Monsef H, Smith S E. A new approach for estimating mangrove canopy cover using Landsat 8 imagery[J]. Computers and Electronics in Agriculture, 2017, 135: 183-194.
10. Shi L, Fang J, Zhao Y. Automatic shadow detection in high-resolution multispectral remote sensing images[J]. Computers and Electrical Engineering, 2023, 105: 108557.
11. Wang X, Voytenko D, Holland D M. Accuracy evaluation of digital elevation models derived from Terrestrial Radar Interferometer over Helheim Glacier, Greenland[J]. Remote Sensing of Environment, 2022, 268: 112759.
12. Ward G J, Wang T, Geisler-Moroder D, et al. Modeling specular transmission of complex fenestration systems with data-driven BSDFs[J]. Building and Environment, 2021, 196: 107774.
13. Du H, Chen X, Xi J. An improved background segmentation algorithm for fringe projection profilometry based on Otsu method[J]. Optics Communications, 2019, 453: 124206.
14. Fu H, Zhou T, Sun C. Object-based shadow index via illumination intensity from high resolution satellite images over urban areas[J]. Sensors, 2020, 20(4): 1077.
15. Hou S W, Sun W F, Zheng X S. Overview of cloud detection methods in remote sensing images[J]. Space Electronic Technology, 2014, 11(3): 68-76.
16. Liu Z, Yang J, Wang W, et al. Cloud detection methods for remote sensing images: a survey[J]. Chinese Space Science and Technology, 2023, 43(1): 1.
17. Mahajan S, Fataniya B. Cloud detection methodologies: Variants and developmentA review[J]. Complex & Intelligent Systems, 2020, 6: 251-261.
18. Siddiq S, Kaur K, Dhir R. Automatic Detection of Cloudy and Non-Cloudy SAR Images Using Convolutional Neural Networks[C]//2023 Third International Conference on Secure Cyber Computing and Communication (ICSCCC). IEEE, 2023: 350-355.
19. Scaramuzza P L, Bouchard M A, Dwyer J L. Development of the Landsat data continuity mission cloud-cover assessment algorithms[J]. IEEE Transactions on Geoscience and Remote Sensing, 2011, 50(4): 1140-1154.
20. Zhu Z, Woodcock C E. Object-based cloud and cloud shadow detection in Landsat imagery[J]. Remote sensing of environment, 2012, 118: 83-94.
21. Yin S, Wang L, Wang Q, et al. M2F2-RCNN: Multi-functional faster RCNN based on multi-scale feature fusion for region search in remote sensing images[J]. Computer Science and Information Systems, 2023 (00): 54-54.
22. Zhu Z, Woodcock C E. Automated cloud, cloud shadow, and snow detection in multitemporal Landsat data: An algorithm designed specifically for monitoring land cover change[J]. Remote Sensing of Environment, 2014, 152: 217-234.
23. Teng L, Qiao Y, Shafiq M, et al. FLPK-BiSeNet: Federated Learning Based on Priori Knowledge and Bilateral Segmentation Network for Image Edge Extraction[J]. IEEE Transactions on Network and Service Management, 2023.
24. Xie F, Shi M, Shi Z, et al. Multilevel cloud detection in remote sensing images based on deep learning[J]. IEEE Journal of Selected Topics in Applied Earth Observations and Remote Sensing, 2017, 10(8): 3631-3640.
25. Qiu S, Zhu Z, He B. Fmask 4.0: Improved cloud and cloud shadow detection in Landsats 4C8 and Sentinel-2 imagery[J]. Remote Sensing of Environment, 2019, 231: 111205.

26. Chang H, Fan X, Huo L, et al. Improving Cloud Detection in WFV Images Onboard Chinese GF-1/6 Satellite[J]. Remote Sensing, 2023, 15(21): 5229.
27. Xu D, Li X, Zhao L, et al. Hyperspectral Remote Sensing Image Cloud Detection Based on Spectral Analysis and Dynamic Fractal Dimension[J]. Laser & Optoelectronics Progress, 2019, 56(10): 101003.
28. Calin M A, Calin A C, Nicolae D N. Application of airborne and spaceborne hyperspectral imaging techniques for atmospheric research: Past, present, and future[J]. Applied Spectroscopy Reviews, 2021, 56(4): 289-323.
29. Zhang H, Huang Q, Zhai H, et al. Multi-temporal cloud detection based on robust PCA for optical remote sensing imagery[J]. Computers and Electronics in Agriculture, 2021, 188: 106342.
30. Zhang Y, Yang C, Tao R, et al. Multi-temporal Cloud Detection Method for Qinghai-Tibet Plateau based with FY-4A Data[J]. Remote Sensing Technology and Application, 2020, 35(2): 389-398.
31. Khoomboon S, Kasetkasem T, Rakwatin P. A land cover mapping algorithm for thin to medium cloud-covered remote sensing images using a level set method[J]. International Journal of Remote Sensing, 2022, 43(10): 3803-3842.
32. Candra D S, Phinn S, Scarth P. Automated cloud and cloud-shadow masking for Landsat 8 using multitemporal images in a variety of environments[J]. Remote Sensing, 2019, 11(17): 2060.
33. Zhang X, Liu L, Chen X, et al. A novel multitemporal cloud and cloud shadow detection method using the integrated cloud Z-scores model[J]. IEEE Journal of Selected Topics in Applied Earth Observations and Remote Sensing, 2019, 12(1): 123-134.
34. Yin S. Object Detection Based on Deep Learning: A Brief Review[J]. IJLAI Transactions on Science and Engineering, 2023, 1(02): 1-6.
35. Zhu X, Gao F, Liu D, et al. A modified neighborhood similar pixel interpolator approach for removing thick clouds in Landsat images[J]. IEEE Geoscience and Remote Sensing Letters, 2011, 9(3): 521-525.
36. Liu M, Liu X, Li J, et al. Evaluating total inorganic nitrogen in coastal waters through fusion of multi-temporal RADARSAT-2 and optical imagery using random forest algorithm[J]. International journal of applied earth observation and geoinformation, 2014, 33: 192-202.
37. Huang S, Ding J, Liu B, et al. The capability of integrating optical and microwave data for detecting soil moisture in an oasis region[J]. Remote Sensing, 2020, 12(9): 1358.
38. Li T, Cheng X. Estimating daily full-coverage surface ozone concentration using satellite observations and a spatiotemporally embedded deep learning approach[J]. International Journal of Applied Earth Observation and Geoinformation, 2021, 101: 102356.
39. Ji S, Dai P, Lu M, et al. Simultaneous cloud detection and removal from bitemporal remote sensing images using cascade convolutional neural networks[J]. IEEE Transactions on Geoscience and Remote Sensing, 2020, 59(1): 732-748.
40. Abdullah A S S, Abed M A, Al Barazanchi I. Improving face recognition by elman neural network using curvelet transform and HSI color space[J]. Periodicals of Engineering and Natural Sciences, 2019, 7(2): 430-437.
41. Yin S, Li H. Hot region selection based on selective search and modified fuzzy C-means in remote sensing images[J]. IEEE Journal of Selected Topics in Applied Earth Observations and Remote Sensing, 2020, 13: 5862-5871.
42. LI Z W, ZHENG W, FANG J, et al. Optimizing suitability area of underwater gravity matching navigation based on a new principal component weighted average normalization method[J]. Chinese Journal of Geophysics, 2019, 62(9): 3269-3278.
43. Jia Y L, Zhang W, Meng L K. A study of selection method of NDWI segmentation threshold for GF1 image[J]. Remote Sensing for Land and Resources, 2019, 31(01): 95-100.
44. Hu Q, Wu W, Xia T, et al. Exploring the use of Google Earth imagery and object-based methods in land use/cover mapping[J]. Remote Sensing, 2013, 5(11): 6026-6042.

45. Amani M, Ghorbanian A, Ahmadi S A, et al. Google earth engine cloud computing platform for remote sensing big data applications: A comprehensive review[J]. IEEE Journal of Selected Topics in Applied Earth Observations and Remote Sensing, 2020, 13: 5326-5350.
46. Ding J, Xue N, Xia G S, et al. Object detection in aerial images: A large-scale benchmark and challenges[J]. IEEE transactions on pattern analysis and machine intelligence, 2021, 44(11): 7778-7796.
47. Li D, Wang S, Xiang S, et al. Dual-stream shadow detection network: biologically inspired shadow detection for remote sensing images[J]. Neural Computing and Applications, 2022, 34(12): 10039-10049.
48. Liu D, Zhang J, Wu Y, et al. A shadow detection algorithm based on multiscale spatial attention mechanism for aerial remote sensing images[J]. IEEE Geoscience and Remote Sensing Letters, 2021, 19: 1-5.
49. Alvarado-Robles G, Osornio-Rios R A, Solis-Munoz F J, et al. An approach for shadow detection in aerial images based on multi-channel statistics[J]. IEEE Access, 2021, 9: 34240-34250.

Shoulin Yin received the B.S. and M.S. degrees in image processing from Software College, Shenyang Normal University, Shenyang, China, in 2013 and 2015, respectively. He is currently a PHD with School of Information and Communication Engineering, Harbin Engineering University. He has published more than 20 technical articles in scientific journals and conference proceedings. His research interests include image fusion, object detection, and image recognition. Email:yslin@hit.edu.com.

Liguo Wang received his M.A. degree in 2002 and Ph.D. degree in signal and information processing in 2005 from Harbin Institute of Technology, Harbin, China. He held postdoctoral research position from 2006 to 2008 in the College of Information and Communications Engineering, Harbin Engineering University. He is currently a Professor with Information and Communications Engineering, Dalian Minzu University, Dalian, China. His research interests are remote sensing image processing and machine learning. He has published three books, 27 patents, and more than 200 papers in journals and conference proceedings. Email: wangliguo@hrbeu.edu.cn.

Lin Teng received the M.A. degree in computer application technology from Shenyang Normal University, Shenyang, China, in 2020. She is currently working toward the Ph.D. degree in communication engineering with the College of Information and Communication Engineering, Harbin Engineering University, Harbin, China. Her research interests include image processing and semantic segmentation.

Received: December 30, 2023; Accepted: April 20, 2024.